Editors' Suggestion

Doping of $BiFeO_3$: A comprehensive study on substitutional doping

Julian Gebhardt* and Andrew M. Rappe
Department of Chemistry, University of Pennsylvania, Philadelphia, Pennsylvania 19104, USA

(Received 6 December 2017; published 5 September 2018)

We investigate the effects of metal dopants on $BiFeO_3$ (BFO) by first-principles calculations. Substitutional doping in oxide materials is often complicated by the formation of defects that interfere with, dominate, or otherwise change the effects of the introduced dopant. As a result, extracting correct conclusions and working principles experimentally requires extensive characterization of the material properties, which is not easily accessible. We solve this problem by an extensive model study of the changes that are introduced in the crystal, electronic, and magnetic structure of BFO, focusing on substitutional doping in an otherwise ideal crystal. We examine a large number of candidate elements. From our results, trends can be established within rows and groups of the periodic table. We predict the preferred doping site (Bi or Fe substitution) and oxidation state for each dopant and provide an in-depth understanding of the structural and electronic changes that are introduced upon doping. From this, we are able to divide the periodic table into direct p dopants, n dopants, and isovalent cases. For the latter, understanding the valence configuration and the band structure of the doped systems enables us to distinguish between isovalent dopants that can enable p-type, n-type, or no doping. A comparison of the resulting acceptor and donor states provides insight into the performance of such dopants and, together with defect formation energies, enables ranking all candidates and identification of optimal dopants.

DOI: 10.1103/PhysRevB.98.125202

I. INTRODUCTION

$BiFeO_3$ (BFO) has been intensively studied over the last decades. It has high Curie ($T_C = 1123$ K) and Néel temperatures ($T_N = 643$ K) and, therefore, is both ferroelectric and antiferromagnetic at room temperature [1]. Due to this multiferroic behavior, it is seen as a promising future material for oxide memory devices [2]. Materials such as BFO are of great general interest in the rich field of oxide electronics that could enable more evolved functionality beyond Boolean computing, up to adaptive functionality [3]. In order to realize oxide electronics, pn junctions are vital. BFO has the perovskite (ABO_3) structure, with Bi^{+3} and Fe^{+3} cations on the A and B site, respectively. Enveloping the cations, O^{2-} anions form FeO_6 octahedra and BiO_{12} cuboctahedra. In principle, both cations can be substituted by other metals. For example, introducing a dopant atom M in oxidation state $i = \frac{2y}{x}$, substituting Bi^{+3} in an A site, can generally be described via

$$\mathrm{Bi}_A^{+3} + \frac{1}{x} M_x \mathrm{O}_y \longrightarrow \frac{1}{2}\mathrm{Bi}_2\mathrm{O}_3 + M_A^{+i} + \left(\frac{i-3}{4}\right)\mathrm{O}_2 + (3-i)h^+ , \quad (1)$$

and an analogous expression for Fe^{+3} substitution in a B site. Thus, depending on i, substitutional doping results in $(3-i)$ charge carriers and electron (e^-) doping (n-type), hole (h^+) doping (p-type), or isovalent doping:

$$i : \begin{cases} > 3\ ;\ (i-3)e^-\ ;\ n \text{ doping} \\ = 3\ ;\ (\text{isovalent}) \\ < 3\ ;\ (3-i)h^+\ ;\ p \text{ doping} \end{cases} . \quad (2)$$

However, doping experiments in oxide materials are often complicated by the formation or presence of other defects. For example, oxygen vacancies create n-type doping, turning even BFO p-type doped with Ca^{+2} to an n-type material [4]. On the other hand, cation vacancies ($v'''_{Bi/Fe}$) create p-type doping [5]. Thus, controlling the defect chemistry in doped oxides is vital; otherwise, the effects of defects will overlay, alter, or completely change the desired effects of substitutional doping. For example, this can be seen in a study that discusses the alloying of BFO with $Bi_{0.5}K_{0.5}TiO_3$ where no effect of the two dopants (K^+ and Ti^{+4}) is observed [6]. Instead, a change between n and p doping is attributed to the presence of oxygen and bismuth vacancies, respectively. As a result, p-type doping by substitutional cation doping is challenging and has so far only been reported for Ca^{+2} [4] and Ba^{+2} [7]. The accurate control and determination of chemical composition in oxides is challenging, especially for cations. In addition, since defect-rich materials are prone to low conductivity, crystalline oxides that are altered via substitutional doping (but otherwise defect free) are the target materials that are likely to be best suited for oxide electronic applications. Therefore, we provide a model study for such well-controlled systems, discussing the effects of many metal dopants on both the A and B site in otherwise defect-free BFO.

A huge number of doping studies have already been carried out in BFO (see references in Fig. 1). In fact, nowadays, dopant studies can be found that almost span the entire periodic table. The presence of oxygen vacancies in most experimental

*jugeb@sas.upenn.edu

 ©2018 American Physical Society

Li^{+} [52]	Be												
Na^{+} [51]	Mg											Al^{+3} [46, 53]	
K	Ca^{+2} [8–11]	Sc^{+3} [12, 13]	Ti^{+4} [14–17]	V^{+5} [17, 18]	Cr^{+3} [19–22]	+2-4 Mn [22–29]	Fe^{+3}	Co^{+3} [30, 31]	Ni^{+3} [32, 33]	+2-3 Cu [17, 32]	Zn^{+2} [16, 17]	Ga^{+3} [34, 35]	Ge
Rb	Sr^{+2} [9, 10]	Y^{+3} [36, 37]	Zr^{+4} [38]	Nb^{+5} [26]	+4-6 Mo [39, 40]	Tc	+3-5 Ru [41]	Rh	Pd^{+2} [42]	Ag^{+} [32, 43]	Cd	In	Sn^{+4} [44]
Cs	Ba^{+2} [45–47]	Lu^{+3} [48]	Hf	Ta^{+5} [49]	W	Re	Os	Ir	Pt	Au	Hg	Tl	Pb^{+2} [10, 50]

FIG. 1. Periodic table of metallic elements (including Ge) without lanthanoids and actinoids. Elements that have been considered as dopants in BFO are marked *A* (red) or *B* (blue and white stripes) according to their preferred doping site. Although we provide a rather comprehensive list of previous works, the cited references are by no means complete, and studies that include more than one dopant were not listed for each element. For elements where different oxidation states were reported previously, a range is given. (See also Refs. [8–53].)

samples, however, led most researchers to focus on doping as a tool to reduce the resulting leakage currents in undoped BFO. As a result, the detailed mechanisms and effects of defect-induced transport are not often studied, and most transport studies focus on intrinsic defects [5]. Therefore, and due to the sheer amount of (mostly) isolated studies on single (or small selections of) dopants that were conducted in a trial and error fashion (Fig. 1), guidance via theoretical studies and a fundamental understanding of the effects introduced by substitutional metal doping appears to be overdue, in order to inform and guide materials design. Herein, we fill this void by considering a very broad set of metals. Since *p*-type doping by cations has been more challenging in the past, with only few successful experimental protocols [4,7,43] due to the omnipresence of oxygen vacancies in experimental samples, we focus especially on metals that have a chance to form M^{+i} cations with $i < 3$. Nevertheless, we also consider $i \geqslant 3$ iso- and aliovalent dopants in order to discuss all possible doping effects. We explain in detail the effects that each category of dopants has on the electronic structure of pristine BFO. We find that doping effects indeed follow the considerations of Eq. (2). The resulting holes or excess electrons for $i \neq 3$ dopants are mainly localized on iron centers as assessed by geometrical changes and analysis of the electronic structure. The detailed distribution of holes onto the surrounding ions depends on the oxidation state i of the dopant and its lattice site. For most transition metals, we observe isovalent doping. The various different valence *d*-shell configurations lead to different electronic structures with impurity levels introduced either as additional acceptor or donor levels in the band gap, as partially occupied bands at the Fermi level, or as bands that are located energetically away from the edge states, with little influence on the electronic structure. *n* dopants lead to partly-filled bands at the Fermi level, suggesting that substitutional cation doping is not a suitable strategy for *n*-doped semiconductors. A variety of different dopants are thermodynamically accessible for both cation lattice sites. The computed site preference can be related to interpolated ionic radii [54]. In addition to formation energies, the relative energetic positions of the introduced acceptor/donor levels gives insight into the performance of each dopant and enables us to suggest ideal candidates for each doping type. The differences with respect to induced magnetism, crystal structure, and acceptor level of dopants and their doping site provide a catalog of BFO modifications for various applications.

II. COMPUTATIONAL DETAILS

A pseudocubic ($2 \times 2 \times 2$) BFO cell is constructed from a converged primitive unit cell in the R3c phase [55]. For structural relaxation and initial electronic structure results we use density-functional theory (DFT) with the Perdew-Burke-Ernzerhof (PBE) generalized gradient approximation (GGA) [56], as implemented in the QUANTUM ESPRESSO package [57]. Total energies are relaxed to 3×10^{-7} eV/cell and crystal structures (all degrees of freedom, atomic positions, and cell) until forces on ions are below 0.005 eV/Å and the pressure on the unit cell is below 0.5 kbar. Note that due to this full structural relaxation, additional corrections in the charged calculations in the spirit of Ref. [58] cannot be considered. However, for materials with large dielectric constant such as BFO ($\epsilon' = 54$) [59], these corrections can be expected to be small. In these calculations, core electrons are treated by different flavors of pseudopotential schemes, compiled in the optimized and tested STANDARD SOLID STATE PSEUDOPOTENTIAL database [60,61]. Wave functions are expanded in a large plane-wave basis with an energy cutoff of 1360 eV in order to guarantee converged results without the necessity of conducting convergence tests for each case. The Brillouin zone is sampled by a $3 \times 3 \times 3$ Monkhorst-Pack **k**-point grid [62]. See Ref. [63] for further details and an assessment of the convergence of the setup.

From this optimized cell, *A*- and *B*-site doped systems were created by substitution of one bismuth or iron atom with the target dopant, followed by full reoptimization of the crystal structure. Note that in the chosen unit cell this does not model the dilute limit. On one hand, this reflects the large concentration of dopants that is often found in experiments. On the other hand, this allows us to study the induced effects at their extreme limit, enabling us to distinguish between different dopants. At the same time, the obtained qualitative effects and trends are unlikely to differ drastically for smaller dopant concentrations. In order to confirm this, we performed test calculations for Li and Cs doping in a larger ($4 \times 4 \times 4$) unit cell (see section S1). We can show that the geometry, doping effect, and optical properties remain unchanged, whereas thermal excitation and formation energies quantitatively depend on the defect density. The decreasing trend of the latter suggests that attractive defect-defect interactions may lead to clustering of defects even in dilute samples. Further studies are necessary to clarify this in detail for dopants of interest.

In all cases, the G-type antiferromagnetic spin structure of Fe atoms (see Sec. III A) was chosen as starting point and found in the optimized structures. Magnetic moments of other elements (including dopants) were initialized to zero and determined iteratively.

PBE predicts partially-filled bands for many dopants. We attribute this to a prominent weakness of GGAs, causing too small band gaps. We, therefore, rely on a more evolved description using a fraction of (screened) exact exchange *via* the HSE06 functional [64] with 25% Hartree-Fock (HF)

exchange and a screening parameter ω of 0.07 $Å^{-1}$. These calculations were carried out for the PBE-optimized geometries, employing the FRITZ HABER INSTITUTE AB INITIO MOLECULAR SIMULATIONS package [65]. In independent tests on the bulk metals as well as elemental oxygen, we find that the "tight" parameters, with a further increase of the default basis set to "tier2" for iron and bismuth, are required to guarantee accurate results with cohesive energies converged to 0.01 eV/atom. However, the band gap of BFO is reasonably well converged (to 0.04 eV) between this extensive protocol and the default "light" setup and basis. We, therefore, use the latter throughout this study. Throughout the text, band structures and densities of states (DOS) are shown for this computational setup.

For the evaluation of doping energies [see Eq. (3) below], we also compute the total energies of binary oxides for all considered dopants, choosing the oxidation state that we find for each element as dopant in BFO (with a few exceptions where the required oxide is not known or unstable). We chose these as systematic reference energies over the wide range of dopants, because these binary oxides are often used for fabricating doped oxide films. Structures were taken from the inorganic crystal structure database [66] and fully optimized at the PBE level with the same setup as in the plane-wave calculations above. Monkhorst-Pack grids for these calculations were selected individually for each case to yield converged total energies within 0.01 eV/atom. The setup and structure references can be found in Table SI of the Supplemental Material (SM) [67].

III. RESULTS

A commonly used practice in perovskite doping is to aim for metal ions with an *appropriate* ionic radius, where appropriate is usually interpreted as being as close as possible to the ionic radius of the ion that is going to be replaced. On one hand, this seems straightforward; on the other hand perovskites are known to be structurally rather flexible, accepting tolerance factors [68] in a range of roughly $0.75 < t < 1$ [69]. In the case of BFO, the host material itself is slightly off from an ideal tolerance factor itself. Note that we use ionic radii after Shannon and Prewitt [54], extrapolated to the correct coordination numbers (see Table SII), whereas smaller values are often used for elements where an ionic radius for twelvefold coordination is not reported. Our analysis of ionic radii shows that linear extrapolation to twelvefold coordination can overestimate the resulting ionic radius by up to 8%. Therefore, the tolerance factor for BFO should be within $t = 0.94$–0.99. Nevertheless, we use the linear interpolated values throughout, providing an upper bound for all elements treated on the same footing. The BFO tolerance factor smaller than one means that ion sizes different from Fe^{+3} and Bi^{+3} are not necessarily destabilizing to the structure and could, to some extent, even be favorable. Therefore, we keep our study, at least for the initial steps, as broad as possible, in order not to miss possible candidates and also to be able to deduce more general trends than possible from a more confined set of dopants. The list of metal ions included in our study is summarized in Fig. 2, together with the preferred substitution site and oxidation state. It spans a wide range of elements and different oxidation states. For each case, we test

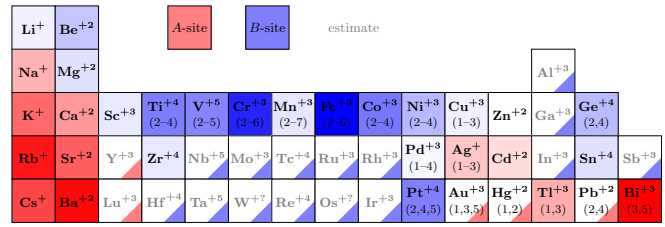

FIG. 2. Metallic elements (including Ge and Sb). Panels of elements (black text) considered in this study as dopants are filled red (A) or blue (B) representing their preferred doping site according to our DFT calculations. The intensity of the color indicates the strength of the thermodynamic preference toward one site. Other elements (gray text) are not treated explicitly, but their effects can be estimated from the collected data. The observed oxidation state as dopant in BFO is given as superscript to each element. For elements that are known to exist in various oxidation states, the typical range of oxidation states is given in brackets below the elemental symbol. The site preference is only indicated in the lower right corner if it was not explicitly confirmed by computation. In these cases, site preference is estimated from ionic radii considerations and trends within the periodic table.

at least the substitution site that is more reasonable according to ionic radii, although in all cases where the mismatch is not expected to be too large, both sites were considered for completeness.

A. Pristine $BiFeO_3$ and doping

We briefly introduce BFO and its electronic properties (Fig. 3) to set the stage for the remainder of this study. The perovskite structure of BFO is shown in Fig. 3(c). Substitutional doping is considered by replacing one A- or B-site atom by dopant atom M, denoted as M_A or M_B, respectively.

Undoped BFO is a nearly direct semiconductor with a band gap of 1.1 eV at the PBE level (in good agreement with earlier results) [70]. This, of course, is an underestimation, which can be corrected to give more realistic, larger band gaps *via* a Hubbard term (reported values of 1.3–1.9 eV) [71], the inclusion of (screened) exact exchange (reported values of 2.1–3.6 eV) [72–74], or many-body GW calculations (3.6 eV [75]). Experimentally, the optical gap is observed to be of the order of 2.1–2.8 eV, depending on the exact reaction conditions, phase, and film thickness [76–82]. We use the screened exact exchange approach, providing a corrected electronic structure description via the HSE functional (see computational details). We obtain a slightly too large direct band gap at the **K** point of 3.17 eV [Fig. 3(a)], which is well in between earlier results using exact exchange and many-body theory.

The (G-type) antiferromagnetic structure has mostly spin degenerate bands, with only small deviations observed along **M** to **S** [Fig. 3(a)]. Thus, the density of states [Fig. 3(b)] is spin up-down symmetric. The VB region contains mostly oxygen $2p$ contribution. Some iron d contribution is distributed over the range of oxygen-dominated bands (down to ≈6 eV below the Fermi level) indicating chemical bonding. However, the majority of the partly-filled $3d^5$ shell of the Fe^{+3} cations is located about 8 eV below the Fermi level, with alternating iron centers contributing to opposing spin channels. The CB region is dominated by the empty fraction of the partly-filled

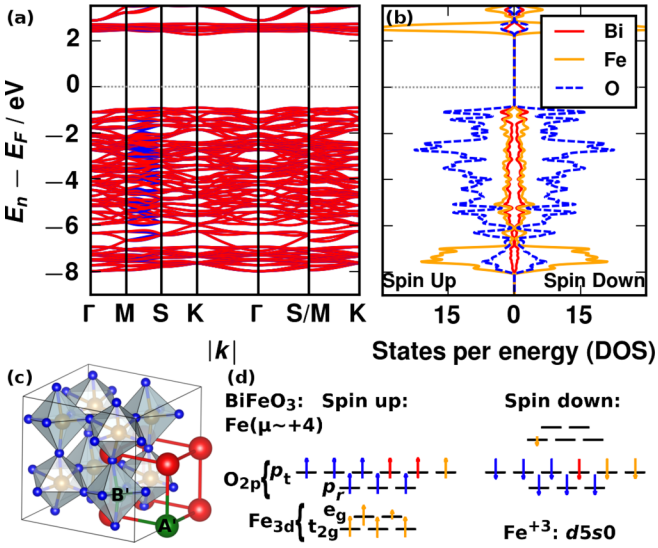

FIG. 3. Spin-polarized HSE band structure [(a), blue spin up, red spin down] and DOS (b) of pristine (undoped) BFO are referenced here and in the following to the (numerically determined) Fermi level (E_F, gray dashed line). Inset (c) shows the perovskite structure with A-site Bi^{+3} (red), B-site Fe^{+3} (orange), and O^{2-} (blue) ions in a pseudocubic unit cell. Dopant positions A' and B' in this cell, resulting (individually) in a doping concentration of 12.5%, are colored green and labeled accordingly. Contributions to bands in DOSs are colored according to the color of atomic species in geometry (c) throughout, unless noted otherwise. (d) Simplified valence electron shell configuration of one $BiFeO_3$ unit, showing the nine oxygen bands (three radial orbitals p_r oriented towards the iron center and six tangential orbitals p_t perpendicular to that; completely filled due to three additional electrons from Bi^{+3} and Fe^{+3} each) and the iron $3d$ valence shell for both spin components for the example of a spin-up polarized iron center. Schematic electron affiliation to ions is indicated by the respective color.

iron d orbitals. Thus, the region around the Fermi level is dominated by the BO_6 octahedra, with little contribution from the A-site cations, in line with the expected electronic structure for a transition-metal perovskite. The main results of the DOS are summarized schematically (without taking orbital hybridization into account correctly for simplicity) in Fig. 3(d), showing the valence electron filling for one $BiFeO_3$ unit with nine valence oxygen $2p$ orbitals (split into six p_t and three p_r states) and the iron $3d$ shell (split into e_g and t_{2g} states) for both spin components. The oxygen $2p$ levels are filled by the respective oxygen valence electrons (blue) as well as three electrons from the two $+3$ cations (red and orange). The remaining $BiFeO_3$ units yield analogous diagrams for iron centers that are spin up (down) polarized [spin up polarization is shown in Fig. 3(d)]. Since every iron center has a magnetic moment of about 4 μ_B, half of an electron schematically occupies the unoccupied fraction of the iron d states. These kinds of diagrams will be used to summarize the effects of substitutional doping in the following, supplementing the discussed DOS.

In the following, we present results for doped BFO, focusing on the preferred doping site and the induced electronic effect. Throughout the text, the energy of doping according to Eq. (1) is evaluated by [5,83,84]

$$E_{\text{doping},q}(M_{\text{Bi/Fe}}) = E(\text{BFO@}M_{\text{Bi/Fe},q}) + \mu(\text{Bi/Fe}) - E(\text{BFO}_q) - \mu(M) + q(\epsilon_{\text{VBE}} + E_F^{'}) , \quad (3)$$

with the energies of pristine BFO [$E(\text{BFO}_q)$] and BFO substitutionally doped with one metal ion M in a lattice site A = Bi or B = Fe and charge state q [$E(\text{BFO@}M_{\text{Bi/Fe}_q})$]. ϵ_{VBE} and $E_F^{'}$ are the energy of the VBE of the undoped system at the HSE level and the defect energy level, which is a parameter tuned within the band gap to account for different conditions and to determine when a specific defect state becomes filled. Due to the many considered dopants, we chose $q = 0$ throughout our study but analyze the influence of the charged state for alkali and alkali-earth metal dopants. As references, we chose binary oxides for each cation, computing the chemical potentials for metals $\mu(M)$ according to

$$\mu(M) = [E(M_xO_y) - y\mu(\text{O})]/x , \quad (4)$$

with the required oxygen reference obtained from

$$\mu(\text{O}) = [E(\text{O}_2) - E_{\text{corr}}]/2 . \quad (5)$$

The correction term for μ(O) was determined to correct for the known inherent overbinding of GGA methods for O_2 [85] in order to reproduce the experimental O_2 atomization energy of 5.17 eV [86]. The required correction term was evaluated to be 1.02 eV, in agreement with similar procedures [32,87]. As mentioned above, we are interested here in model systems that do not interact with other defects.

B. Alkali metals

We start our discussion for neutral defects $q = 0$. Replacing a Bi^{+3} A-site or a Fe^{+3} B-site ion by any alkali metal results in a band structure with two acceptor bands in the band gap. Representative band structures and DOS are shown in Fig. 4 for the cases of lithium and cesium doping in their preferred lattice sites. For a comparison with the other alkali metals, see Fig. S1. For doping on either site, acceptor bands are created in one spin channel, which exclusively exhibit BFO band character. Just like undoped BFO, the VB and CB regions are dominated by oxygen and iron bands, respectively, and the alkali-metal dopant character is located further away from the Fermi level.

The emergence of these acceptor bands can be explained by the formation of a dopant in oxidation state $+1$ (M^+) and the creation of two holes [Eq. (2)]. Since alkali-metal dopants can only provide one valence electron, two oxygen states at the valence band edge (VBE) would be unoccupied in the doped BFO unit [Fig. 4(g)]. Interestingly, we observe that these hole states are localized on iron centers in the $BiFeO_3$ units that are surrounding the defect, leading to the observed acceptor states with mixed iron and oxygen character. The detailed mechanism of this charge redistribution differs for the two doping sites in the number of FeO_6 octahedra that are involved: For B-site substitution [Figs. 4(b) and 4(c)], two iron centers (black) adjacent to the dopant contribute to the acceptor states, whereas only one iron center is involved in the case of A-site substitution [Figs. 4(e) and 4(f)]. Besides the observed changes in the DOSs, we also observe this charge

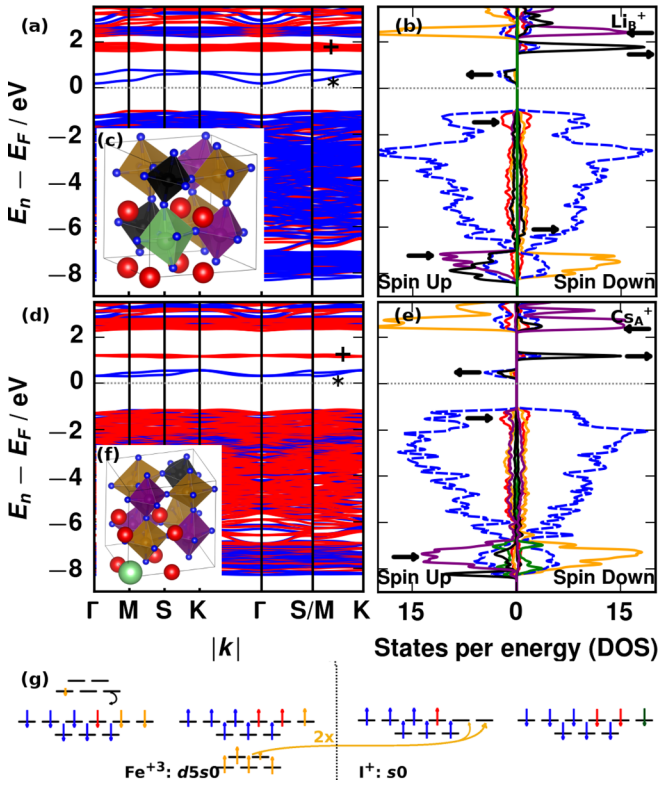

FIG. 4. Band structure, DOS, and structure for Li_B^+ (a)–(c) and Cs_A^+ (d)–(f) doped BFO. Atoms are represented as blue (O), red (Bi), green (dopant M^{+i}), orange (Fe with spin-down magnetization), purple (Fe with spin-up magnetization), and black (Fe with spin-up magnetization with reduced electron charge) spheres, respectively. Contributions to states in the DOS are colored accordingly. Changes in the DOS for the oxidized iron center compared to the other iron centers of the same magnetization are indicated by black arrows. In both cases, two acceptor bands with FeO_6 band character emerge, indicating Fe oxidation. Besides the direct doping effect in the spin channel opposite to the incorporated dopant, an indirect effect is observed for the CBs of the same iron centers in the other spin channel. Bands arising in the band gap due to the direct or the indirect effect are marked by an asterisk (*) or a plus sign (+), respectively. Scheme (g) indicates the doping effect for alkali-metal M_B^+ substitution: The d shell is absent and two holes are formed in the $BiMO_3$ unit, which are filled by two neighboring $BiFeO_3$ units.

depletion by investigating the FeO_6 octahedra. The octahedral volumes of the iron centers that constitute the acceptor states are reduced. This suggests the oxidation of the corresponding Fe^{+3} cations to higher oxidation states. Furthermore, Mulliken and Bader [88] charge analysis reveals that electron density is reduced on the six oxygen atoms of the respective FeO_6 octahedra compared to other oxygen atoms and the undoped case. Such a combined reduction of Bader charges of oxidized metal centers and their oxygen surrounding has been observed previously [89]. These findings are in line with the mixed iron and oxygen character of the emerging acceptor bands.

In addition to the discussed depopulation of two former VBs (direct doping effect) in one spin channel, we also observe a change in the iron dominated CBs in the other spin channel. The empty bands of oxidized $BiFeO_3$ units appear in the band gap, below the CB that is dominated by the other iron centers. This change can be attributed to the increased attraction of energy levels by the oxidized iron core, due to the reduced screening of the positive charge for iron in higher oxidation states. In summary, this means that holes are created in the FeO_6 octahedra rather than on the dopant or its surrounding oxygens for all alkali metals. This is because the partly-filled iron $3d$ levels (and the oxygen $2p$ states) are energetically close to the VBE, whereas filled core-level states of alkali-metal M^+ ions are located at much lower energies. This leads to the depletion of charge in one FeO_6 octahedron and the formal oxidation of one Fe^{+3} to Fe^{+5} for A-site doping and two Fe^{+3} to Fe^{+4} for B-site doping, yielding similar acceptor bands with iron and oxygen character for both cases.

Overall, A- and B-site substitution yield similar electronic structures. The doped electronic structures are not spin symmetric, due to the different effects on iron and oxygen states in both spin channels. However, this is an artifact of modeling one dopant per unit cell, i.e., we observe antiferromagnetic structures when two dopants replace spin-inequivalent ions in the unit cell. The magnetic moment that is introduced by alkali-metal dopants depends on the doping site. On one hand, this might appear straightforward, since introducing an M^+ defect with zero magnetic moment replaces either another nonmagnetic element (bismuth on the A site) or a magnetic iron center with a magnetic moment of roughly 4 μ_B (B-site substitution). The effects are, however, complicated by the oxidation state of the dopant and the observed oxidation of iron centers. For A-site substitution, removing two electrons from a single iron center reduces its magnetic moment, leading overall to a magnetization of 2 μ_B per unit cell. This is different for B-site substitution, where a dopant replaces one magnetic iron center in one spin channel, leading to a magnetization of the cell. As a result, iron oxidation leads to the removal of two electrons from iron centers that are spin polarized in the opposite direction and overall a magnetic moment of 3 μ_B is observed per unit cell (see also discussion below). This demonstrates that the substitution site plays an important role and that if a maximal magnetic moment is required by a target application, B-site substitution is preferable for alkali-metal dopants.

Separation and width of the two types of emerging states within the band gap (depopulated former VBs and downshifted CBs) depend on the dopant atom. A small increase of the band gap from 2.91 to 2.99 eV, accompanied by a lifting of the acceptor bands from 1.45 eV above the VBE to 1.61 eV, is observed along Na^+ to Rb^+ (see Fig. S1), indicating that smaller ions lead to shallower acceptor levels. Comparing lithium substitution on the A site with the B site, the acceptor level is raised by 0.13 eV for iron substitution. Thus, in terms of the doping effect, A-site substitution seems to be preferable. This again demonstrates the importance of the substitutional site. The latter can be potentially controlled by the choice of experimental growth conditions if the site preference is not too large, as is the case for Li^+ (see below).

We now discuss the site preference for alkali-metal substitution in BFO, comparing DFT results with estimates from ionic radii (Table I). Since B-site doping forms a M^+O_6 octahedron, this structure is unlikely for the generally large +1 cations and, in case of the alkali metals, limited to Li^+. All larger alkali metals thermodynamically favor A-site substitution,

TABLE I. Doping energies as defined in Eq. (3) for A- and B-site substitution of the tested dopants. †The respective binary oxide is not stable or well studied. CoO and PdO were used as reference instead.

M^{+i}	$E_{\text{doping}}(M_A)$/eV	$E_{\text{doping}}(M_B)$/eV
Li^{+}	−1.25	−1.36
Na^{+}	−2.15	−1.54
K^{+}	−2.34	−1.17
Rb^{+}	−2.04	−0.22
Cs^{+}	−1.37	0.09
Ag^{+}	−0.67	−0.23
Be^{+2}	0.82	0.37
Mg^{+2}	0.17	−0.08
Ca^{+2}	−0.91	−0.10
Sr^{+2}	−1.28	−0.01
Ba^{+2}	−1.37	0.56
Zn^{+2}	0.02	0.02
Cd^{+2}	−0.24	0.04
Hg^{+2}	0.17	
Pb^{+2}	−0.43	
Sc^{+3}	0.82	0.64
Cr^{+3}	2.08	0.35
Mn^{+3}	0.55	0.35
$Co^{+3\dagger}$	0.23	−0.84
Ni^{+3}	0.72	0.16
Cu^{+3}	0.25	0.12
$Pd^{+3\dagger}$	0.51	0.45
Au^{+3}	1.82	
Tl^{+3}	0.46	1.10
Ti^{+4}	2.73	1.72
Zr^{+4}	2.58	2.41
Pt^{+4}	1.87	1.73
Ge^{+4}	2.39	1.84
Sn^{+4}	2.34	2.10
V^{+5}	4.07	3.11

and for Li the B-site preference is small. We find that the preferred adsorption site can be predicted by ionic radii, with Li^{+} as only alkali metal favoring B-site substitution and Na^{+} already being too large, favoring the A site. However, relative energy differences are not monotonically related to size. Due to the changes in iron oxidation states and accompanied FeO_6 octahedral volumes, doping energies do not quite follow trends that would be deduced from ionic radii. For example, Na^{+} would exhibit the smallest deviation from any host cation (only −0.06 Å smaller than Bi^{+3}), but K_{Bi}^{+} has the lowest doping energy, due to the best balance of ion size, required structural changes due to iron center oxidation, and electronic effects. Therefore, relying solely on ionic radii when choosing ideal doping candidates is not a sufficient strategy, but further analysis, e.g., based on first-principles calculations, is required. Incorporation of alkali metals into BFO from binary oxides is generally thermodynamically favorable. Na, K, and Rb are fairly close in energy and are energetically favorable by ≈0.7 eV over Li and Cs, indicating that the latter are too small and too large for the A-site, respectively. Nevertheless, A-site substitution in BFO seems to be possible for a quite large range of ionic radii from 1.53–1.86 Å. Interestingly, the difference between Cs and Bi (0.43 Å) is a factor of four larger than the difference between Li and Fe (0.11 Å), both yielding, however, almost identical doping energies. This indicates that larger cations are tolerated more easily on the A site. This again shows the importance of first-principles calculations and can be rationalized with a tolerance factor below one for the pristine material, i.e., the fact that Bi^{+3} ions are slightly too small.

Compared to the discussed p doped limit for $q = 0$, considering charged systems allows us to model situations where electrons are exchanged with a bath. For example, in the case of p-type doping, $q = -1$ ($q = -2$) corresponds to a situation in which one (two) acceptor band(s) are occupied, and the oxidation of iron centers becomes obsolete. The doping energies for alkali metals with varying q are compared in Fig. S2 for the more favorable adsorption site. Except for Li_B^{+}, all cases show that $q = 0$ is the thermodynamic favorable structure in the p-type doping limit $E_F^{'} = 0$. Na, K, and Rb show a direct transition to $q = -2$ at $\approx E_F^{'} = 1$ eV. For Li, $q = -1$ is stabilized and the transition from $q = -1$ to $q = -2$ is located in the CB. This appears to be an interesting consequence from the different oxidation mechanism of iron centers for B-site substitution. Analogous findings are also found for alkali-earth metal cases Be and Ba. Since we are mostly interested in the respective doping type limit of each dopant, we proceed with discussing $q = 0$ for all cases, noting that B-site substitution may favor a charged state of $q = -1$.

C. Alkaline-earth metals

The observed doping effect for alkaline-earth metals is similar to the alkali metals, but only one acceptor band is observed instead of two. This can be explained by a different oxidation state of +2, with M^{+2} alkaline-earth metal dopants contributing two electrons to the VBs, i.e., only one hole is introduced. We show the electronic structure of Mg- and Ca-doped BFO in Fig. 5 (see Fig. S2 for a comparison with the other alkaline-earth metal doped cases). Again, no contribution of the dopant orbitals is observed in the acceptor band, i.e., it has mixed iron and oxygen character. This means, similar to alkali metals, holes are not localized in the low-lying valence orbitals of alkaline-earth metal +2 dopants, but lead to a depopulation of one BFO VB, which can be attributed to a neighboring $BiFeO_3$ unit. This can be interpreted as the oxidation of one Fe^{+3} center to Fe^{+4}. As a secondary effect, bands from the oxidized iron center are shifted below the CBE in the other spin channel. In line with having only introduced one hole, this effect is less pronounced compared to M^{+} alkali-metal defects, leading to a smaller stabilization of the unoccupied iron states and a larger distance to the doping-induced acceptor states. The localization of the introduced hole is again in line with structural changes and charge density analysis. The oxygen octahedron of the oxidized iron center is smaller and the charge density is decreased at the respective oxygen atoms. Comparing A- and B-site substitution, the acceptor band generally shows larger band dispersion for A-site doping.

Comparing the energetic positions of the acceptor levels, we again observe a small destabilization of the acceptor level for larger ions from periods three to five. As for alkali metals, elements from periods two and six deviate from this trend, showing a stabilization of the acceptor band for barium and

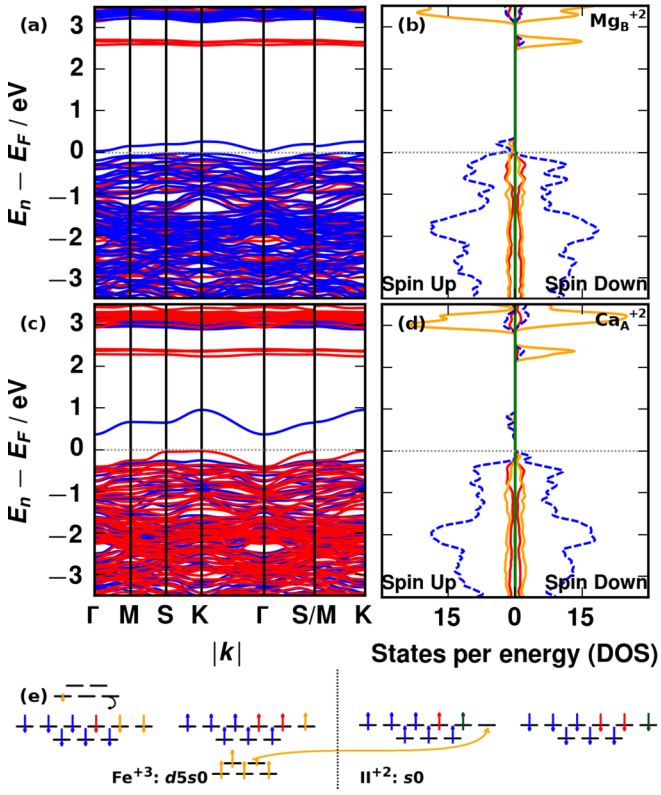

FIG. 5. Band structure and DOS for Mg_B^{+2} (a),(b) and Ca_A^{+2} (c),(d), respectively. In both cases, an acceptor band emerges due to the introduced hole doping, leading to the depopulation of one VB with mixed oxygen and iron character located at a neighboring FeO_6 octahedron. The observed charge depletion can be interpreted as iron oxidation to Fe^{+4}, which is accompanied by the stabilization of iron states below the CBE. Similar to alkali-metal doping, no contribution of the dopant is found in the vicinity of the band gap. (e) Schematic valence orbital filling for B-site substitution, displaying the doped $BiMO_3$ and the oxidized neighboring $BiFeO_3$ unit.

a destabilization for beryllium doping. Mg^{+2} results in the shallowest acceptor level of all tested materials. Compared to alkali-metal doping, the introduced acceptor levels are stabilized by roughly 1 eV, allowing for efficient p-type doping via thermal excitation, in line with the reports on successful p doping of BFO by Ca^{+2} [4,90]. Our results suggest, however, that magnesium and barium can provide even better p doping.

The magnetic moment introduced per dopant atom again depends on the substitutional site. On the A site, the resulting magnetic moment is reduced compared to alkali metals to a magnetic moment per cell of 1 μ_B. B-site substitution by an alkaline-earth metal, however, creates a much larger magnetic moment of 4 μ_B.

Energetically, B-site formation becomes more favorable due to the smaller ion size of M^{+2} compared to M^+ ions. Consequently, Be^{+2} strongly favors B-site substitution and even Mg^{+2} from the third period is favorable in the B site, in line with predicted ionic radii differences (Table SII) and resulting smaller $M^{+2}O_6$ octahedra compared to M^+ doping. Thus, the transition to favor the A site occurs one period later compared to alkali metals, with Ca^{+2} being almost of the same size as Na^+. Doping energies also closely follow this trend of ionic radii. Generally, dopant formation becomes thermodynamically more stable with decreasing mismatch between ionic radii of the dopants and either Fe^{+3} or Bi^{+3} ions (see discussion below). However, this trend is not always fulfilled: While Ba^{+2} is too large for the A site and Sr^{+2} would fit almost perfectly, Ba^{+2} is energetically favored.

Comparing alkaline-earth with alkali-metal dopants, doping energies are overall reduced, the latter being stabilized by up to ≈1.6 eV per dopant. This trend, however, decreases for increasing periods, and doping with elements of the sixth period (Ba^{+2} and Cs^+) is isoenergetic. The general trend of preferring M^+ over M^{+2} indicates a tendency to form holes in this material. However, the evaluated doping energies are also dependent on the chosen oxide references, which are generally more stable in higher oxidation states. These energetic effects compete with size effects, since the larger alkali M^+ ions have optimal ion sizes in different periods than alkaline-earth M^{+2} ions. For example, while Li^+ is 0.09 Å too large for the B site, Be^{+2} is 0.2 Å too small. In line with previous observations, the large energy difference of 1.73 eV in favor of Li^+ substitution indicates that ions that are too large for a lattice site are energetically favorable over ions that are too small, but also suggests an additional electronic effect.

In summary, this means that alkaline-earth metal doping is favorable over alkali-metal doping in terms of p-doping efficiency due to shallower doping levels and also if one seeks to generate large magnetic moments. The formation of alkaline-earth metal defects, however, is thermodynamically less favorable. Nevertheless, all dopants should be feasible to be introduced into BFO (Be^{+2} in the stabilized $q = -1$ state). Ba^{+2} and particularly Mg^{+2} have shallower acceptor levels than Ca^{+2} and, thus, should be able to yield enhanced p doping.

D. Transition metals

Transition metals span a wide range of oxidation states and different d-shell configurations, leading to a variety of effects on the electronic structure.

1. First row

The effects of first-row transition metal doping in BFO are collected in Figs. 6–8. Many of the transition metals are known to exist in a variety of oxidation states (Fig. 2), and some researchers have examined multiple oxidation states as BFO dopant (see Fig. 1). This demonstrates that the correct valence shell filling cannot be easily deduced from simple electron counting arguments but requires in-depth analysis. Despite the fact that an integer oxidation state cannot always be assigned based on standard methods that rely on projecting the electron density onto a set of localized orbitals or a Bader analysis [91], our calculations allow us to assign oxidation states clearly to most transition metals. Cases with a partial filling of bands at the Fermi level can be assigned to a fractional oxidation state.

Scandium adopts oxidation state +3 [Figs. 6(a)–6(c)], in order to fill the oxygen-dominated VBs. Its empty d shell is observed roughly 6 eV above the CBE, i.e., no defect levels contribute to the edge states, resulting in a band structure very similar to undoped BFO. Titanium also empties its valence d shell, leading to an oxidation state of +4 [Figs. 6(d)–6(f)]. The

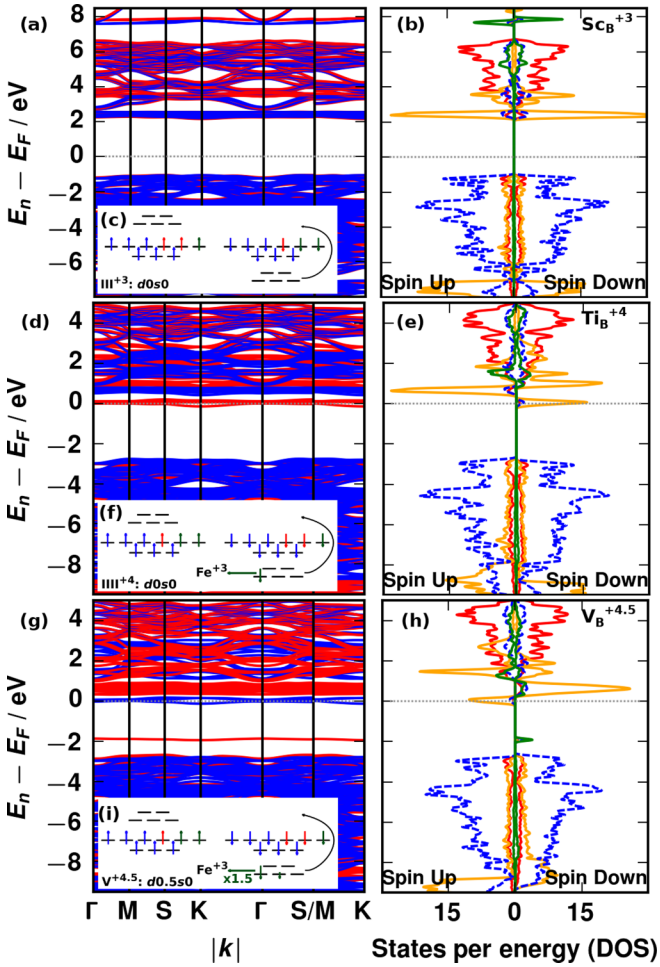

FIG. 6. Band structure, DOS, and schematic filling of the valence shell for Sc_B^{+3} (a)–(c), Ti_B^{+4} (d)–(f), and $V_B^{+4.5}$ (g)–(i), respectively. Different d-shell configurations and effects on the electronic structure are observed. Sc^{+3}: Empty d shell, *i.e.*, no impurity state in the band gap. Ti^{+4}: One excess electron is localized on one neighboring $BiFeO_3$ unit, in order to keep an empty titanium d shell, leading to n doping. $V^{+4.5}$: Similar to Ti^{+4}. The additional electron leads to an occupied impurity level above the VBE, in addition to the observed n doping. This d electron appears to be partly located on surrounding $BiFeO_3$ units, leading to a fractional oxidation state for this metallic system (see text for details).

excess electron occupies iron bands at the CBE, i.e., we observe n-type doping. This is also in line with structural changes and a charge density analysis. The $Ti^{+4}O_6$ octahedron is considerably smaller than the $Sc^{+3}O_6$ octahedron. In addition, FeO_6 octahedra are enlarged in order to accommodate the excess electron, which is also confirmed by an increase of electron density on the oxygen atoms. In contrast to the discussed localization of holes above, this excess electron appears to be distributed over three FeO_6 octahedra, indicating a fractional reduction of the respective iron centers rather than a clear reduction of a single iron center towards Fe^{+2}. This is in line with the downshift of three iron CBs toward the Fermi level. Overall, titanium doping leads to a metallic system with one filled CB and two additional bands very close to the Fermi level (one partly filled, see Fig. S4). Hence, despite successful n-type doping, titanium substitution promotes a semiconductor to metal transition undesirable for the envisioned semiconductor devices.

The band structure and DOS for vanadium doping [Figs. 6(g)–6(i)] are similar to the Ti^{+4} case. However, we observe one defect state above the VBE, indicating that some charge remains in the vanadium $3d$ shell. Comparing the structural changes, VO_6 is smaller than $Ti^{+4}O_6$, and larger FeO_6 octahedra are observed for vanadium doping. Together this suggests a higher oxidation state for vanadium, with only fractional occupation of one impurity d state. This is in line with the band structure that shows a much larger filling of the partially-filled second CB at the Fermi edge compared to Ti^{+4} (Fig. S4). This can be explained by the known tendency of transition metals to form d^0 over d^1 configurations [92]. In summary, our data suggest an oxidation state between +4 and +5 for vanadium dopants.

Vanadium is the first of the first-row transition metals that exhibits dopant d band contribution to filled states around the Fermi level. From group six on, all transition metals have a partly-filled d shell, impacting the electronic and magnetic structure. Chromium is a M^{+3} dopant, with d^3 configuration [Figs. 7(a)–7(c)]. The occupied impurity d states are located above the VBE, enabling very weak n doping. Otherwise, the electronic structure of pristine BFO is mainly retained. We also do not observe noticeable changes in the FeO_6 octahedra or oxygen oxidation states, in line with isovalent doping. The additional valence electron of manganese leads to a mostly filled d shell in one spin channel, with a partly occupied impurity state at the Fermi level [Figs. 7(d)–7(f)]. This means that the tendency to form a stable d^5 configuration leads to an oxidation state of about +3 and a high-spin d^4 configuration. Cobalt is also observed in an oxidation state of +3 [Figs. 7(g)–7(i)]. Therefore, the resulting band structure is comparable to the other isovalent cases Sc^{+3} and Cr^{+3}. The different d-shell configuration leads to a mostly spin-symmetric DOS, suggesting a low-spin d^6 configuration, in line with a very small CoO_6 volume.

For nickel [Figs. 8(a)–8(c)], we observe three bands above the VB with defect character in one spin channel. They are located in the band gap above the Fermi level, forming rather deep, midgap impurity acceptor states. Such states are unsuitable for thermal excitation as the carrier concentration for the latter is proportional to $\propto e^{-(\Delta\epsilon_A)/k_BT}$, requiring the separation between the valence band energy and the acceptor band $\Delta\epsilon_A$ to be of the order of (a few) k_BT [93]. However, they could be promising for optical applications. All oxygen-dominated VBs are filled, suggesting a Ni^{+3} ion with d^7 valence-shell configuration. Compared to alkali and alkaline-earth metal dopants, the doping effect is significantly different. Acceptor bands do not emerge due to hole formation in VBs from $BiFeO_3$ units, but are impurity states. Consequently, no oxidation of iron centers is observed. Since the acceptor states also have oxygen character due to band hybridization, we observe charge depletion for the oxygen atoms surrounding the nickel defect, similar to what is observed in the oxygen surrounding of oxidized iron centers. Copper [Figs. 8(d)–8(f)] behaves similarly to Ni^{+3} and is also observed in oxidation state +3. Copper d contribution to unoccupied bands is only found in the two acceptor levels that are observed in the

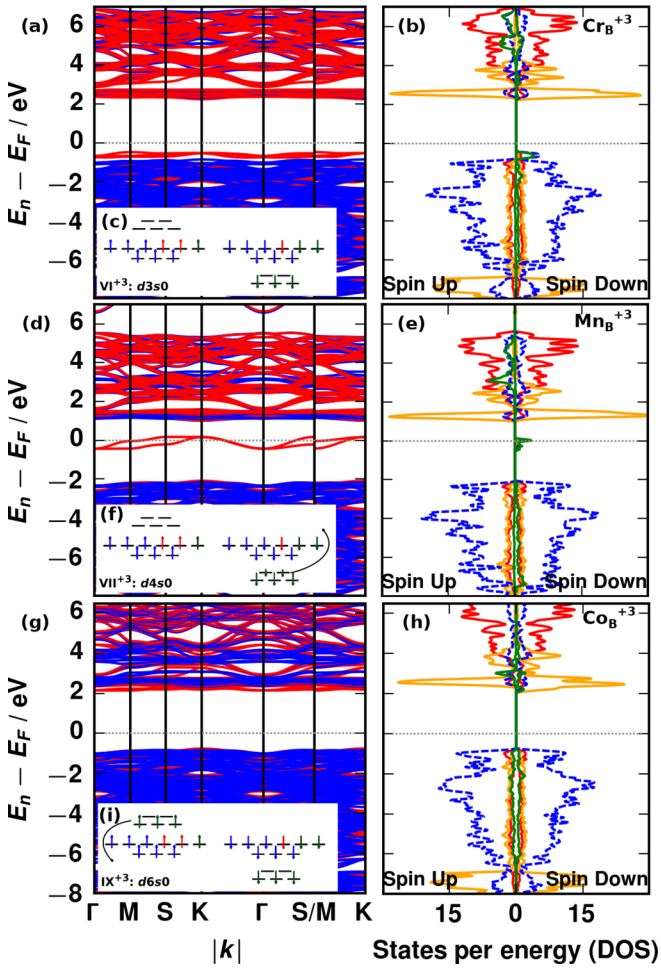

FIG. 7. Band structure, DOS, and schematic filling of the valence shell for Cr_B^{+3} (a)–(c), Mn_B^{+3} (d)–(f), and Co_B^{+3} (g)–(i), respectively. Different d-shell configurations and effects on the electronic structure are observed. Cr^{+3}: d^3 configuration with impurity levels above the VBE. Mn^{+3}: Fractional occupation of d orbitals, due to the stability of a d^5 configuration. This leads to a partly-filled impurity level at the Fermi level. Co^{+3}: Low-spin d^6 configuration, with no impurity acceptor or donor states.

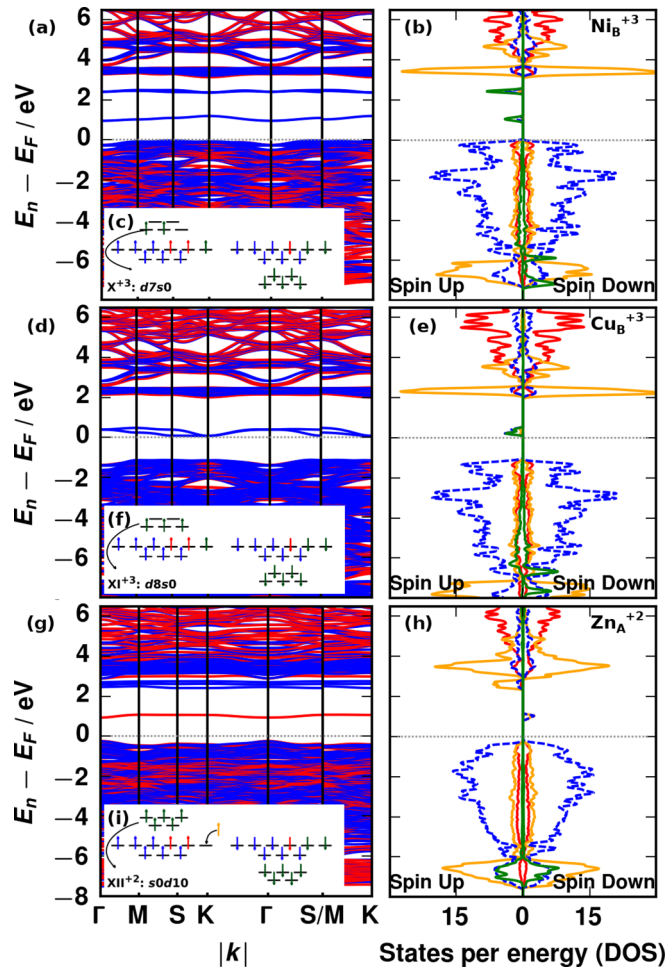

FIG. 8. Band structure, DOS, and schematic filling of the valence shell for Ni_B^{+3} (a)–(c), Cu_B^{+3} (d)–(f), and Zn_A^{+2} (g)–(i), respectively. Different d-shell configurations and effects on the electronic structure are observed. Ni^{+3}: Three acceptor bands in the band gap, which can be attributed to empty nickel d orbitals, enabling hole conduction. Cu^{+3}: Similar to nickel with one additional electron occupying the dopant d shell. Two impurity bands in the band gap that can act as acceptor bands for hole doping. Zn^{+2}: Filled d shell resulting in one hole, located at a neighboring $BiFeO_3$ unit. The resulting oxidation of the iron center is similar to alkaline-earth metal doping.

band gap. This indicates a d^8 configuration, in line with the additional electron compared to Ni^{+3}. Cu^{+3} substitution is also accompanied by empty midgap impurity states above the VBE. As for nickel, band mixing of the impurity states with oxygen orbitals leads to an observable charge depletion of MO_6 oxygen ions. We observe just one acceptor band in the band gap of zinc-doped BFO [Fig. 8(g)]. This band has mixed iron and oxygen character, whereas all dopant d bands are observed to be filled and spin paired below the oxygen-dominated VBs. In contrast to iron and other transition-metal dopants, no zinc $3d$ hybridization with the oxygen VBs is observed. This indicates a filled d^{10} configuration for zinc [Figs. 8(h) and 8(i)], i.e., zinc in an oxidation state of +2. Consequently, a hole is introduced, leading to the observed acceptor band. Similar to alkaline-earth metal doping, this hole is located on a neighboring $BiFeO_3$ unit. This means that the acceptor band has mixed iron and oxygen, character, and we observe the oxidation of one iron center to Fe^{+4} as above (reduced octahedron volume, charge depletion at oxygen atoms, and downshift of the respective iron bands below the CBE).

All first-row transition state metals but Zn^{+2} prefer B-site substitution, in line with their ionic radii similar to Fe^{+3}. Thermodynamically, doping is unfavorable for transition metals in higher oxidation states. This is in line with the large band gap of BFO, since n doping requires the (fractional) filling of the CBE.

To sum up the first row of the transition metals, d block elements favor stable d-shell configurations. This means d^0 for groups III to V (note that group V, i.e., vanadium, is not completely obeying this rule, according to our discussion above) and d^{10} for group XII. The other transition elements adopt the most stable configurations they can, trying to completely or half fill the t_{2g} or e_g subsets. This means d^3 for group VI, d^4 for VII (note again the fractional occupation for manganese),

d^6 for a low-spin configuration in group IX, d^7 for group X, and d^8 for group XI. Only group XII (Zn^{+2}) behaves similarly to groups I and II *p*-type doping. Groups X and XI are isovalent dopants that introduce deep acceptor impurity levels within the band gap. Other transition metals are isovalent dopants with no or very weak doping effects or direct *n*-type dopants that result in fractional occupation of the iron CBs. As such, they cause a semiconductor to metal transition.

2. Second row

We now turn our discussion to the second row of transition metals. Comparing titanium with zirconium doping (Fig. S5), very similar electronic structures are observed, i.e., *n*-type doping with occupied iron CBs due to a +4 oxidation state of the dopant. In line with estimated tolerance factors from ionic radii, we observe that Zr^{+4} also favors the *B* site. Due to the identical behavior of group IIII metals, we expect other second-row transition metals to behave analogously to their group member of the first transition metal row, since most corresponding elements of the first and second rows are found in the same oxidation states. Thus, yttrium through rhodium are likely to form small ions in high oxidation states that prefer the *B* site (except Y^{+3}) and that lead to isovalent and metallic *n*-type dopants analogously to the first row elements. Therefore, we focus on group X to XII elements, i.e., Pd through Cd.

Despite a recent report that suggests an oxidation state of +2 for palladium defects in BFO [42], we observe palladium in an oxidation state of +3, similar to Ni^{+3}. Here, however, we observe two acceptor bands and one additional occupied band above the former VBE [Fig. 9(a)]. The DOS in Fig. 9(b) shows that palladium *d* character is found in both acceptor levels and in the iron-dominated CBE. This suggests a low-spin d^7 configuration, in contrast to the high-spin result of Ni^{+3} [Fig. 9(c)]. The oxygen contributions to the unoccupied defect bands lead again to an observable charge depletion at oxygen atoms of the MO_6 octahedron. Pd^{+3} also prefers *B*-site substitution. However, the mismatch of ionic radii with Fe^{+3} is larger compared to Cu^{+3} and, therefore, Pd^{+3} substitution is thermodynamically less favorable.

The silver-doped band structure [Fig. 9(d)] appears similar to the Cu^{+3} case, with two acceptor levels in the band gap that have comparable band dispersion as for copper. However, on close inspection of the DOS [Fig. 9(e)], we find significant differences. The acceptor bands have mixed iron and oxygen character and no silver contribution is observed in any unoccupied band close to the CBE. This suggests a different *d*-shell configuration of d^{10} [Fig. 9(c)]. This is confirmed by closely inspecting contributions to bands from group XI elements (see Fig. S6). We find only *s* and *p* contributions to unoccupied bands for silver, whereas copper and gold exhibit distinct *d* character in the two acceptor levels.

The d^{10} configuration of silver suggests a different oxidation state of +1, compared to Cu^{+3}. As evident by the DOS, the two holes are not localized in the $AgFeO_3$ unit but on two neighboring $BiFeO_3$ units instead. This is in perfect agreement with the observed decrease of the size of one FeO_6 octahedron and accompanied electron depletion of the respective oxygen atoms. In other words, we observe iron center oxidation and

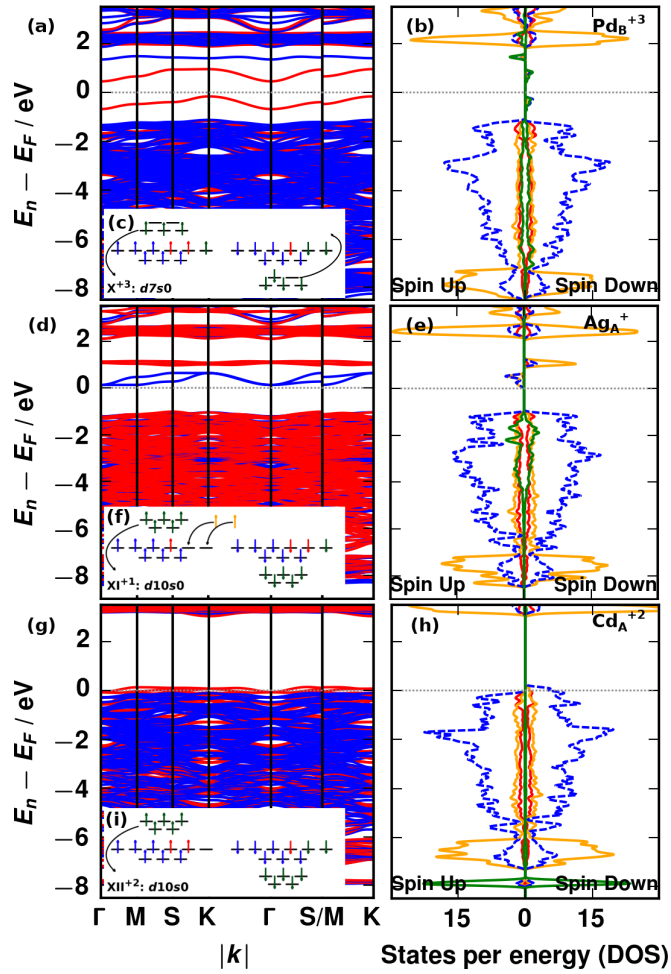

FIG. 9. Band structure, DOS, and schematic filling of the valence shell for Pd_B^{+3} (a)–(c), Ag_A^{+} (d)–(f), and Cd_A^{+2} (g)–(i), respectively. Pd^{+3}: Dopant *d* character is found in three empty states. In contrast to Ni^{+3}, some *d* band character is found in the iron-dominated CBE, leading to only two visible acceptor impurity states in the band gap region. In addition, one occupied defect state is observed above the VBE. Ag^{+}: Different oxidation state compared to Cu^{+3}, despite similarities in the band structure. Therefore, d^{10} configuration leading to two holes that are localized on two neighboring $BiFeO_3$ units analogously to alkali metal doping. Cd^{+2}: Filled d^{10} shell, even lower than for Zn^{+2}. The different localization of the hole leads to a partly unoccupied oxygen band at the VBE.

effects on the electronic structure identical to the case of alkali-metal dopants at the *A* site. Consequently, this is again accompanied by a downshift of iron bands below the CBE. We observe *A*-site preference for Ag^{+} substitution, in line with the large ionic radius of Ag^{+}. Compared to the alkali metal of similar size (Rb^{+}), the thermodynamic preference for *A*-site substitutional doping is reduced by more than a factor of two (−0.67 eV vs −2.04 eV), which can be attributed to the much higher electronegativity of silver compared to alkali metals.

Differences are observed comparing the band structures of group XII dopants zinc and cadmium [Fig. 9(g)]. Instead of an acceptor level in the band gap, a partly-filled band is observed at the Fermi level in the case of cadmium. The DOS in Fig. 9(h) shows symmetric, deep cadmium *d* bands, indicating

a d^{10} configuration, as for Zn^{+2} [Fig. 9(i)]. The resulting hole, however, is located in the $CdFeO_3$ unit rather than a neighboring $BiFeO_3$ unit, leading to the depopulation of the oxygen-dominated VBE. This is in line with a partial depletion of charge from the oxygen atoms of the CdO_{12} cuboctahedron that have the smallest bonding distances to the Cd^{+2} ion. In summary, this means that, despite the introduction of a hole, cadmium doping does not lead to a p-doped semiconductor, due to the different location of the hole compared to other M^{+2} dopants. The increased ionic radius of Cd^{+2} compared to Zn^{+2} results in a clear preference for A-site substitution. Finally, we also treat the third row of transition metals (sixth period) analogously to the second row. The obtained results are in line with the first- and second-row transition metals and the data can be found in the SM (see Fig. S7 and the corresponding discussion).

In summary, all M^{+i} dopants with $d^m, 0 < m < 10$, dopant d bands contribute to impurity bands around the Fermi level. These can either act as additional donor levels below the Fermi level, additional acceptor levels above the Fermi level, or as partly-filled states at the Fermi level. As a result, we find isovalent dopants that tune the band gap suitable for optical applications (Ni^{+3}, Cu^{+3}, Pd^{+3}, and Au^{+3}). These midgap levels differ in band character compared to the defect levels induced by M^{+} and M^{+2} defects. The subset of transition metals that we find to be n-type dopants all promote a semiconductor to metal transition unsuitable for semiconductor devices.

Transition-metal defects with d^0 and d^{10} configuration do not contribute to edge states. In the case of d^{10} metals, this leads to a hole. This can either result in iron center oxidation analogously to alkali and earth-alkali metal doping (Zn^{+2} and Ag^{+}) or a metallic system with partly occupied oxygen CB (Cd^{+2} and Hg^{+2}).

In terms of formation energies, only Ag^{+}, Co^{+3}, and Cd^{+2} are thermodynamically favorable for the investigated limiting case of $q = 0$. Generally, doping energies are reduced compared to alkaline-earth metals with similar ionic radii (Mg^{+2}–Ca^{+2}). On one hand, this is in line with the trend of thermodynamically favoring dopants in lower oxidation states (alkali metals vs alkaline-earth metals). However, even Ag^{+} is less favorable compared to alkali metals of similar size. In conjunction with the fact that doping effects are predicted to be nonexisting, resulting in metallic systems, or being less efficient than alkaline-earth metal doping, transition-metal doping appears to be less suitable for semiconductor devices.

E. Group XIII

From group XIII elements, only thallium is known to stabilize M^{+i} cations with $i < 3$, whereas aluminum, gallium, and indium are likely to form M^{+3} ions [94]. The band structure of thallium-doped BFO in Fig. 10(a) shows two deep acceptor levels in the band gap. The DOS [Fig. 10(b)] reveals that these bands are dominated by thallium 6s character. This is in line with a Tl^{+3} cation, with filled, deep d shell and empty valence s and p shells. An oxidation state of +3 and the observed impurity levels are also likely to occur for the other group XIII metals. In terms of site preference, only Tl^{+3} is large enough to prefer A-site substitution. Compared to isovalent transition-metal doping, Tl_A^{+3} doping does not introduce a magnetic moment and results in a spin-symmetric DOS.

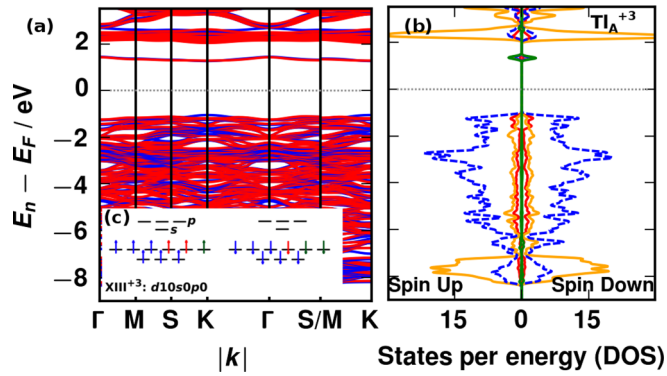

FIG. 10. Band structure (a), DOS (b), and schematic filling of the valence shell (c) for Tl_A^{+3}. Two defect bands with thallium 6s character are observed in the band gap.

F. Group XIV

Group XIV elements are known to have stable +2 oxidation states. Therefore, we test the doping of BFO with germanium through lead. A comparison can be found in Fig. S8. Tin and germanium show partly occupied CBs that can be attributed to the iron-dominated CBE. This means that they are n dopants in an oxidation state of about +4, and the resulting small ions prefer B-site substitution. The effect of lead substitution is shown in Figs. 11(a)–11(c). In contrast to the lighter elements of this group, we observe an acceptor band, which has mixed iron and oxygen contribution. We also observe a mostly spin up-down symmetric DOS, with lead s character contributing to bands 8 eV below the Fermi level. This suggests a $5d^{10}6s^26p^0$ filling, i.e., a Pb^{+2} ion. Thus, in comparison to Tl^{+3}, the Pb valence s shell is filled and only the 6p bands are depopulated. The oxidation state of +2 leads to a hole, which is localized on $BiFeO_3$ units in the vicinity of the dopant similar to alkali and alkaline-earth metals.

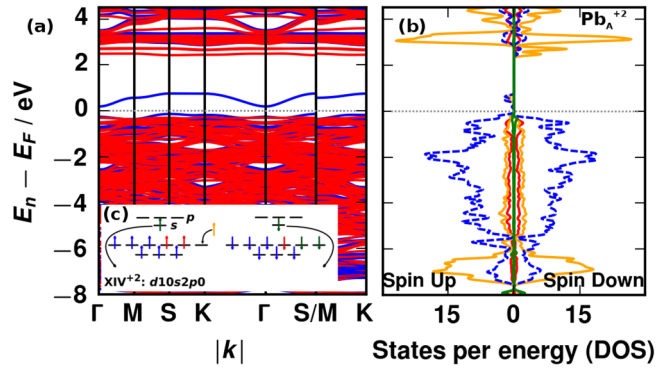

FIG. 11. Band structure (a), DOS (b), and schematic filling of the valence shell (c) for Pb_A^{+2}. The +2 oxidation state leads to a low-lying, filled valence 6s shell (the energetically even lower valence d shell is not displayed). The resulting hole is filled by neighboring $BiFeO_3$ units, leading to the observed acceptor band with mixed oxygen and iron character.

IV. DISCUSSION

A. Electronic effects

For alkali and alkaline-earth metals we find oxidation states of +1 and +2, respectively. Consequently, we obtain desired *p*-type doped semiconductors with one and two holes in the BFO band structure. In the neutral state valid for the *p*-type limit for most cases, these holes are located in $BiFeO_3$ units adjacent to the dopant, which leads to smaller volumes and charge depletion in the respective FeO_6 octahedra, i.e., the oxidation of iron centers. Only a few other cases exhibit such a direct *p*-type doping effect, namely Zn^{+2}, Ag^{+}, and Pb^{+2}. Alternatively, the hole can also be localized at the defect site. This is observed for the heavy elements of group XII (Cd^{+2} and Hg^{+2}). Due to the stabilized and deep valence (*d*) shell in these two cases, the hole is located at the oxygen neighbors of the dopant, leading to a fractional filling of the oxygen-dominated VBE, i.e., a semiconductor to metal transition. Most transition metals adopt a +3 oxidation state and this completely fills the oxygen VBs. The insight from electronic-structure calculations is especially important for these dopants, in order to assign the different *d*-shell configurations correctly and to investigate the resulting different effects on the electronic structure. Transition-metal dopants show a clear tendency toward stable *d*-shell configurations, i.e., d^0 (groups III–V) and d^{10} (group XII). This leads to *n* doping for group IIII and V metals, with excess electrons mainly localized on neighboring FeO_6 octahedra. Consequently, opposite changes compared to *p*-doped cases are observed in the respective FeO_6 octahedra, showing accumulation of additional charge and increased octahedral volume. Transition-metal defects of groups VII through XI (except silver) introduce deep impurity levels in the band gap region, which enables band gap tuning for optical applications. These can be filled impurity donor levels (group VI), or impurity acceptor levels (groups X and XI). Furthermore, fractional occupation of *d* orbitals can lead to metallic behavior (group VII). Group XIII elements also form +3 ions, donating valence *s* and *p* electrons to the oxygen VBs. For Tl^{+3}, we observe unoccupied deep acceptor states. Similarly, group XIV elements donate *s* and *p* electrons, yielding +4 oxidation states and *n* doping. Lead, however, behaves differently, keeping a filled valence *s* shell, resulting in a M^{+2} dopant. In summary, M^{+i} dopants with $i < 3$ are the expected *p*-type dopants and enable (with few exceptions) semiconductors with holes as majority carriers. Isovalent cases are unlikely to contribute to (thermally excited) conduction but can introduce deep impurity states in the band gap. *n*-type doping *via* substitutional cation doping appears less promising, because the nature of the doped band structure significantly differs from the *p*-doped case. While *p*-type doping introduces one or a few acceptor levels close to the VBE, the manifold of iron *d* bands at the CBE leads to fractional occupation and a metallic system for *n*-type doping. Thus, although oxygen vacancies are undesirable as their control is not straightforward under experimental conditions, they could be beneficial or even required for efficient electron transport. In addition, we find that substitution reactions are thermodynamically unfavorable for most isovalent and direct *n* dopants. This means that their successful incorporation in experiments suggests the presence or formation of secondary defects.

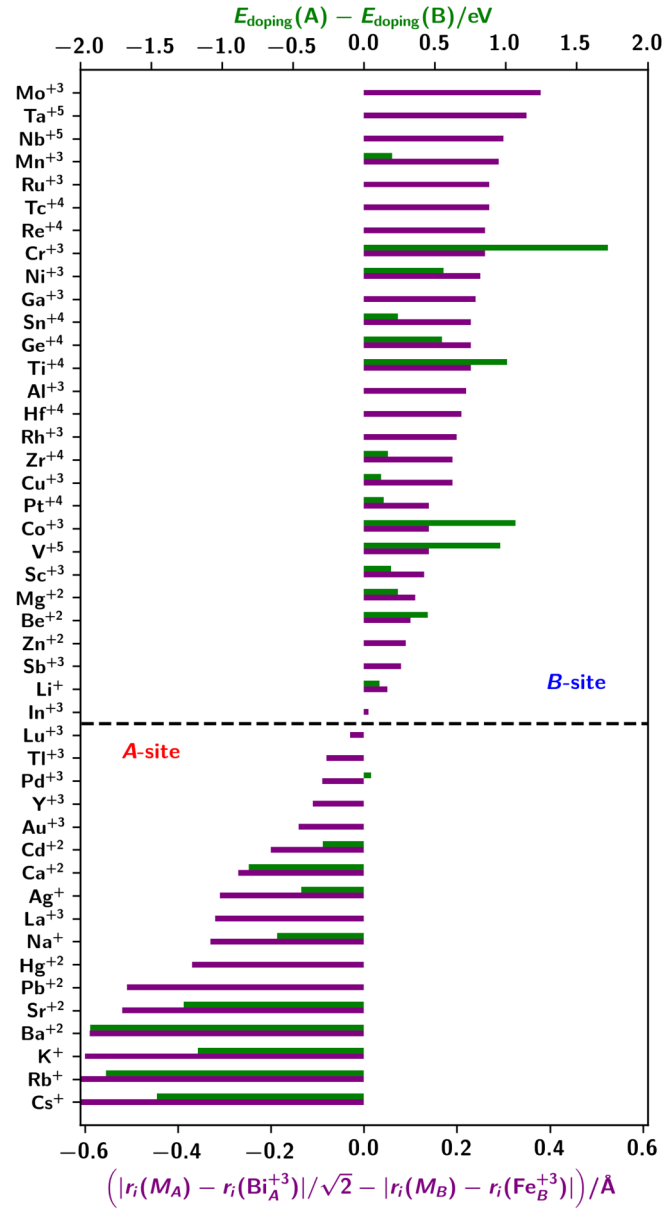

FIG. 12. Site preference for substitutional doping in BFO according to ionic radii (purple) and DFT energies (green). Negative and positive values represent *A*- and *B*-site preference, respectively.

B. Site preference

Once the correct oxidation states are assigned, the site preference between *A*- and *B*-site substitution in BFO can be reliably estimated from differences in the ionic radii between targeted host and dopant ions. We want to stress, however, that the correct oxidation state cannot always be guessed from simple electron counting considerations. Especially for transition metals, but also for other groups, elements are known to stabilize multiple oxidation states (e.g., group XIV), and here first-principles calculations are a valuable tool. The resulting predictions from DFT and ionic radii are compared in Fig. 12. We take into account that misfits in the larger *A* site should lead to a smaller energy penalty, by scaling the ionic radii difference for the *A* site by the idealized Bi/Fe-O bond length difference

of $\sqrt{2}$ (which does not change the qualitative prediction for any case but Lu). By this procedure, only Pd^{+3} is not predicted correctly by ionic radii, which is, however, one of the cases where the site preference is negligibly small. However, the detailed ordering of the site preference energies cannot be predicted reliably from ionic radii and requires first-principles calculations.

Highly oxidized cations in oxidation states of +3 and above prefer the *B* site for most of the periodic table until the sixth period, i.e., up to cations that are almost as large as Bi^{+3} itself. For lower oxidation states, *B*-site preference is limited to a few very light elements (Li, Be, and Mg). However, the fact that metals in low oxidation states can favor the *B* site at all might be surprising and against common perception, e.g., the (small) *B*-site preference of Li^+. All other M^{+i} dopants with $i < 3$ prefer *A*-site substitution.

C. Structural changes

Substitutional doping also promotes various structural changes (see Table SIII). On one hand, there is the direct effect of substituting ions of different sizes. This explains nicely trends of different dopants within one group, e.g., the linear increase of the lattice volume from Li_A^+ to Cs_A^+ doping. Also, some trends among periods can be understood based on different ionic radii, e.g., the fact that alkaline-earth metal +2 doping results in a smaller lattice compared to alkali metal +1 doping within the same period. On the other hand, there are secondary effects due to oxidation (*p*-type doping) or reduction (*n*-type doping) of iron centers that significantly change the oxygen octahedra. As a result, the observed lattice relaxation cannot be directly deduced from ionic radii differences. For example, Na^+ exhibits the smallest mismatch of all alkali metals on the *A* site, however, K^+ and Rb^+ show smaller deviation from the pristine lattice volume (and, thus, more favorable doping energies). This is in line with the oxidation of iron and the resulting decreased spatial requirements of the FeO_6 octahedra. The lattice relaxations show very different behavior. Some dopant cases show uniform expansion/compression along all three lattice vectors (e.g., alkaline-earth metals on the *A* site). Other cases are asymmetrically distorted. This is mainly observed for misfits that are unlikely to exist (e.g., beryllium and dopants in the unfavorable substitution site) but is to a smaller extent also observed for other cases. These kinds of structural distortions could potentially promote phase transitions or enhance ferroelectric properties. In that regard, alkaline-earth metals, Zn, Pd, Pt, Pb, Li_B^+, and Cd_B^{+2} doping are interesting for future studies.

D. Magnetic effects

Replacing ions can also introduce magnetism into antiferromagnetic BFO (see Table SIV). Similar to the structural changes, there are two effects that have to be taken into account. A direct effect naturally occurs when removing a magnetic iron center, leaving the surrounding ions with a magnetic moment opposite to the one of the removed iron atom. Although each iron in BFO has a magnetic moment of approximately 4 μ_B, we find that its removal generally induces a total magnetization of 5 μ_B per cell, in line with the d^5 configuration of iron (e.g., $\mu(\text{BFO-Sc}_B^{+3}) = 5$). Depending on the valence shell configuration of the dopant, the latter may have its own magnetization, which typically aligns with the antiferromagnetic spin structure of the iron sites, reducing the maximally induced magnetism (e.g., $\mu(\text{BFO-Cr}_B^{+3}) = 2$). For all aliovalent dopants, the difference in oxidation state must also be taken into account, since the oxidation/reduction of iron centers generally leads to a reduction of the introduced magnetism. In summary, the magnetism introduced per dopant by substitutional doping on the *B* site in BFO is given by $\mu = 5 - |\mu(M_B^{+i})| - |3 - i|$. When replacing a nonmagnetic Bi^{+3} in the *A* site, substitution alone does not introduce any magnetism. However, the two effects discussed above (magnetism of the dopant and difference in oxidation state) apply, i.e., the magnetic moment induced by *A*-site substitution is given by $\mu = |\mu(M_A^{+i})| + |3 - i|$. The different possibilities with respect to doping site and oxidation state allow us to tune the magnetism that is introduced for each doping type. *p*-type doping can be accompanied by 1 μ_B to 4 μ_B per dopant. Isovalent doping was observed with resulting magnetic moments ranging from 0 μ_B to 5 μ_B. Finally, *n*-type doping can be accompanied by 4 μ_B to 6 μ_B per dopant. Note that the discussed magnetic moments are per dopant per unit cell, i.e., at the current stage we do not investigate ordering effects between dopants. As we have discussed for lithium above, the introduced magnetism can be quenched by dopant-dopant interactions.

E. Dopant variety and implications on defective systems

With this study we demonstrate that the BFO perovskite structure accepts many different ions, even some that have been mostly neglected in previous studies due to ionic radii considerations. Therefore, in addition to well-studied dopants, we also include some dopant elements that have not been recognized as suitable *p* dopants in the field, e.g., alkali and light alkaline-earth metals. Furthermore, we unambiguously narrow down the candidates for *p* doping in BFO to the nonmetallic $i < 3$ cases. Based on our results, we are confident that whenever no *p*-type doping is observed in samples exclusively doped with these suitable candidates, this should be attributed to oxygen vacancies in the experimental samples. Analogously, since *n* doping seems to be accompanied by a semiconductor to metal transition for substitutional dopants, *n*-type semiconducting samples are related to other defects (e.g., oxygen vacancies, not shown).

Different dopants introduce acceptor and donor states at various energies, which are summarized in Fig. 13. The band gap between the oxygen-dominated VB maximum and the iron-dominated CB minimum changes only moderately for most dopants from the undoped BFO. However, the energetic position of the acceptor state relative to the VBE, and, therefore, the first excitation energy, differ greatly. This means that the excitation energy can be adjusted almost continuously from 0.20 eV for Mg_B^{+2} to 2.31 eV for Tl_A^{+3}, which could be interesting for sensors or photovoltaic devices. For semiconductor doping, the distances between acceptor/donor bands and VB/CB, respectively, are a major factor controlling the charge transport efficiency. To that end, *p*-type doping via cation doping seems to be more promising than *n*-type doping, due to

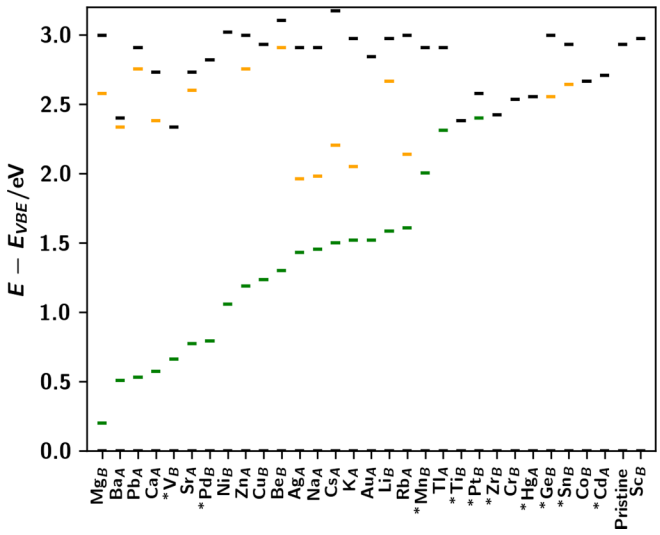

FIG. 13. Energy level comparison for the tested dopants in their most stable substitution site. Displayed is the iron-dominated CBE (black) as well as the maxima of the first acceptor/donor states (green) and the optional shifted iron states (orange) that appear below the CBE in case of iron oxidation. All energies are given relative to the oxygen-dominated VBE. In all cases but n-type doping or partly-filled acceptor bands (indicated by an asterisk), the acceptor band indicates the energy of the first electronic excitation from the VBE.

the already discussed disadvantages in the band structures of n dopants. For p doping, +2 dopants are preferable compared to a +1 oxidation state. Magnesium, barium, and lead +2 should enable the most efficient p-type dopants in that regard. While magnesium and lead might be harder to incorporate into BFO (although still being thermodynamically feasible), Ba^{+2} can be easily incorporated, in line with experimental reports.

V. CONCLUSION

We present an extensive study of substitutional doping in BFO by first-principles calculations, investigating the effects dopants have on the electronic, crystal, and magnetic structure of the host material. We focus on the direct effects of controlled substitutional doping, since such materials can be envisioned to be superior with respect to transport properties compared to materials that contain additional defects.

We show that the doping site preference can be estimated from tabulated ionic radii once the correct oxidation state and coordination number are taken into account. The correct oxidation state and valence shell filling of the dopant and the neighboring iron centers cannot be reliably predicted from simple electron counting arguments, but requires in-depth analysis by, e.g., first-principles calculations.

Our detailed analysis of electronic and crystal structure allows us to identify the most stable substitution site and to classify all tested dopants according to their doping type. Trends within the periodic table are recognized and allow for a prediction of the preferred doping site and the resulting doping effect for all metals. p-type doping is demonstrated to result in holes that can be localized differently. n-type doping can be introduced analogously, but leads to disadvantageous band structures with partly-filled bands at the Fermi level and large gaps below. Thus, controllable n-type doping via metal substitution appears to be challenging and such dopants might require or promote other defects.

Analyzing many dopants allows us to create a catalog that can be chosen from based on formation energy, resulting doping effect, relative energetic position of defect states, induced magnetism, and induced structural changes. This allows us to suggest ideal candidates and should give valuable insight into doping studies in other host materials.

DFT energies show that many dopants can be introduced into BFO starting from binary oxides, and that BFO is a surprisingly flexible host material, allowing ions that considerably deviate from perfect ionic radius requirements. Since detailed structural effects are much more complex than simple ionic radii considerations and are influenced by electronic effects, first-principles calculations are required for a proper analysis of doping in complex oxide materials.

ACKNOWLEDGMENTS

J.G. thanks the German Research Foundation for support from Research Fellowship GE 2827/1-1. A.M.R. acknowledges support from the DOE Office of Basic Energy Sciences, under Grant No. DE-FG02-07ER46431. Computational support is provided by the HPCMO of the U.S. DOD and the National Energy Research Scientific Computing Center of the U.S. DOE.

[1] Y. E. Roginskaya, Y. Y. Tomashpolskii, Y. N. Venevtsev, V. M. Petrov, and G. S. Zhdanov, Sov. Phys. JETP **23**, 47 (1966).
[2] J. F. Scott, Nat. Mater. **6**, 256 (2007).
[3] S. D. Ha and S. Ramanathan, J. Appl. Phys. **110**, 071101 (2011).
[4] N. Masó and A. R. West, Chem. Mater. **24**, 2127 (2012).
[5] Z. Zhang, P. Wu, L. Chen, and J. Wang, Appl. Phys. Lett. **96**, 232906 (2010).
[6] E. T. Wefring, M.-A. Einarsrud, and T. Grande, Phys. Chem. Chem. Phys. **17**, 9420 (2015).
[7] M. Vagadia, A. Ravalia, P. S. Solanki, R. J. Choudhary, D. M. Phase, and D. G. Kuberkar, Appl. Phys. Lett. **103**, 033504 (2013).
[8] N. Gao, C. Quan, Y. Ma, Y. Han, Z. Wu, W. Mao, J. Zhang, J. Yang, X. Li, and W. Huang, Physica B **481**, 45 (2016).
[9] B. Bhushan, A. Basumallick, S. K. Bandopadhyay, N. Y. Vasanthacharya, and D. Das, J. Phys. D: Appl. Phys. **42**, 065004 (2009).
[10] I. O. Troyanchuk, O. S. Mantytskaya, A. N. Chobot, and N. V. Tereshko, Phys. Solid State **51**, 2105 (2009).
[11] K. Kamala Bharathi, W.-M. Lee, J. H. Sung, J. S. Lim, S. J. Kim, K. Chu, J. W. Park, J. H. Song, M.-H. Jo, and C.-H. Yang, Appl. Phys. Lett. **102**, 012908 (2013).
[12] Z. Zhang, P. Wu, L. Chen, and J. Wang, Appl. Phys. Lett. **96**, 012905 (2010).
[13] S. Yasui, H. Uchida, H. Nakaki, K. Nishida, H. Funakubo, and S. Koda, Appl. Phys. Lett. **91**, 022906 (2007).
[14] X. Qi, J. Dho, R. Tomov, M. G. Blamire, and J. L. MacManus-Driscoll, Appl. Phys. Lett. **86**, 062903 (2005).

[15] S. J. Kim, S. H. Han, H. G. Kim, A. Y. Kim, J. S. Kim, and C. I. Cheon, J. Korean Phys. Soc. **56**, 439 (2010).

[16] G. D. Hu, S. H. Fan, C. H. Yang, and W. B. Wu, Appl. Phys. Lett. **92**, 192905 (2008).

[17] P. Kharel, S. Talebi, B. Ramachandran, A. Dixit, V. M. Naik, M. B. Sahana, C. Sudakar, R. Naik, M. S. R. Rao, and G. Lawes, J. Phys.: Condens. Matter **21**, 036001 (2009).

[18] R. Dahiya, A. Agarwal, S. Sanghi, A. Hooda, and P. Godara, J. Magn. Magn. Mater. **385**, 175 (2015).

[19] P. Baettig, C. Ederer, and N. A. Spaldin, Phys. Rev. B **72**, 214105 (2005).

[20] R. Nechache, C. Harnagea, S. Licoccia, E. Traversa, A. Ruediger, A. Pignolet, and F. Rosei, Appl. Phys. Lett. **98**, 202902 (2011).

[21] J. K. Kim, S. S. Kim, W.-J. Kim, A. S. Bhalla, and R. Guo, Appl. Phys. Lett. **88**, 132901 (2006).

[22] H. Naganuma, J. Miura, and S. Okamura, Appl. Phys. Lett. **93**, 052901 (2008).

[23] I. Sosnowska, W. Schäfer, W. Kockelmann, K. H. Andersen, and I. O. Troyanchuk, Appl. Phys. A **74**, s1040 (2002).

[24] S. K. Singh, H. Ishiwara, and K. Maruyama, Appl. Phys. Lett. **88**, 262908 (2006).

[25] S. K. Singh, K. Sato, K. Maruyama, and H. Ishiwara, Jpn. J. Appl. Phys. **45**, L1087 (2006).

[26] C.-F. Chung, J.-P. Lin, and J.-M. Wu, Appl. Phys. Lett. **88**, 242909 (2006).

[27] M. S. Awan, A. S. Bhatti, S. Qing, and C. K. Ong, Key Eng. Mater. **442**, 102 (2010).

[28] I. Sosnowska, W. Schäfer, and I. O. Troyanchuk, Physica B **276-278**, 576 (2000).

[29] J.-Z. Huang, Y. Wang, Y. Lin, M. Li, and C. W. Nan, J. Appl. Phys. **106**, 063911 (2009).

[30] W. Mao, X. Wang, Y. Han, X. Li, Y. Li, Y. Wang, Y. Ma, X. Feng, T. Yang, J. Yang, and W. Huang, J. Alloys Compd. **584**, 520 (2014).

[31] Q. Xu, H. Zai, D. Wu, T. Qiu, and M. X. Xu, Appl. Phys. Lett. **95**, 112510 (2009).

[32] Q. Xu, M. Sobhan, F. Anariba, J. W. C. Ho, Z. Chen, and P. Wu, Phys. Chem. Chem. Phys. **16**, 23089 (2014).

[33] J. Zhao, X. Zhang, S. Liu, W. Zhang, and Z. Liu, J. Alloys Compd. **557**, 120 (2013).

[34] N. Wang, J. Cheng, A. Pyatakov, A. K. Zvezdin, J. F. Li, L. E. Cross, and D. Viehland, Phys. Rev. B **72**, 104434 (2005).

[35] N. Jaber, J. Wolfman, C. Daumont, B. Négulescu, A. Ruyter, G. Feuillard, M. Bavencoffe, J. Fortineau, T. Sauvage, B. Courtois, H. Bouyanfif, J. L. Longuet, C. Autert-Lambert, and F. Gervais, J. Appl. Phys. **117**, 244107 (2015).

[36] A. Mukherjee, S. M. Hossain, M. Pal, and S. Basu, Appl. Nanosci. **2**, 305 (2012).

[37] M. Zhong, N. P. Kumar, E. Sagar, Z. Jian, H. Yemin, and P. V. Reddy, Mater. Chem. Phys. **173**, 126 (2016).

[38] J. Liu, M. Li, Z. Hu, L. Pei, J. Wang, X. Liu, and X. Zhao, Appl. Phys. A **102**, 713 (2011).

[39] Y. Zhang and L.-W. Wang, Phys. Rev. B **83**, 165208 (2011).

[40] D. C. Kundaliya, V. Reeta, R. G. Kulkarni, B. Varughese, A. K. Nigam, and S. K. Malik, J. Appl. Phys. **98**, 013905 (2005).

[41] F. Yan, M.-O. Lai, L. Lu, and T.-J. Zhu, J. Phys. Chem. C **114**, 6994 (2010).

[42] Y. L. Han, W. F. Liu, P. Wu, X. L. Xu, M. C. Guo, G. H. Rao, and S. Y. Wang, J. Alloys Compd. **661**, 115 (2016).

[43] G. M. Albino, O. Perales-Pérez, B. Renteria-Beleño, and Y. Cedeño-Mattei, Mater. Res. Soc. Symp. Proc. **1675**, 105 (2014).

[44] M. Sobhan, Q. Xu, J. Zhao, A. Franklin, Y. Hu, J. S. Tse, and P. Wu, EPL **111**, 18005 (2015).

[45] D. H. Wang, W. C. Goh, M. Ning, and C. K. Ong, Appl. Phys. Lett. **88**, 212907 (2006).

[46] G. Wang, D. Kothari, V. Raghavendra Reddy, and A. Gupta, Phys. Procedia **49**, 199 (2013).

[47] A. R. Makhdoom, M. J. Akhtar, M. A. Rafiq, and M. M. Hassan, Ceram. Int. **38**, 3829 (2012).

[48] C. Nayek, C. Thirmal, A. Pal, and P. Murugavel, Mater. Sci. Eng. B **199**, 121 (2015).

[49] Y.-K. Jun, S. B. Lee, K. Miyoung, S.-H. Hong, J. W. Kim, and K. H. Kim, J. Mater. Res. **22**, 3397 (2007).

[50] V. A. Khomchenko, D. A. Kiselev, M. Kopcewicz, M. Maglione, V. V. Shvartsman, P. Borisov, W. Kleemann, A. M. L. Lopes, Y. G. Pogorelov, J. P. Araujo, R. M. Rubinger, N. A. Sobolev, J. M. Vieira, and A. L. Kholkin, J. Magn. Magn. Mater. **321**, 1692 (2009).

[51] H. Zhang, W. Liu, P. Wu, X. Hai, M. Guo, X. Xi, J. Gao, X. Wang, F. Guo, X. Xu, C. Wang, G. Liu, W. Chu, and S. Wang, Nanoscale **6**, 10831 (2014).

[52] M. M. Shirolkar, C. Hao, X. Dong, T. Guo, L. Zhang, M. Li, and H. Wang, Nanoscale **6**, 4735 (2014).

[53] M. Okada, T. Yoshimura, A. Ashida, and N. Fujimura, Jpn. J. Appl. Phys. **43**, 6609 (2004).

[54] R. D. Shannon and C. T. Prewitt, Acta Cryst. **B25**, 925 (1969).

[55] A. Palewicz, I. Sosnowska, R. Przeniosło, and A. W. Hewat, Acta Phys. Pol. A **117**, 296 (2010).

[56] J. P. Perdew, K. Burke, and M. Ernzerhof, Phys. Rev. Lett. **77**, 3865 (1996).

[57] P. Giannozzi, S. Baroni, N. Bonini, M. Calandra, R. Car, C. Cavazzoni, D. Ceresoli, G. L. Chiarotti, M. Cococcioni, I. Dabo, A. Dal Corso, S. de Gironcoli, S. Fabris, G. Fratesi, R. Gebauer, U. Gerstmann, C. Gougoussis, A. Kokalj, M. Lazzeri, L. Martin-Samos, N. Marzari, F. Mauri, R. Mazzarello, S. Paolini, A. Pasquarello, L. Paulatto, C. Sbraccia, S. Scandolo, G. Sclauzero, A. P. Seitsonen, A. Smogunov, P. Umari, and R. M. Wentzcovitch, J. Phys.: Condens. Matter **21**, 395502 (2009).

[58] C. Freysoldt, J. Neugebauer, and C. G. Van De Walle, Phys. Rev. Lett. **102**, 016402 (2009).

[59] J. Lu, M. Schmidt, P. Lunkenheimer, A. Pimenov, A. A. Mukhin, V. D. Travkin, and A. Loidl, J. Phys.: Conf. Ser. **200**, 012106 (2010).

[60] I. E. Castelli, N. Mounet, A. Marrazzo, G. Prandini, and N. Marzari, Standard Solid State Pseudopotentials (SSSP) (2016).

[61] K. Lejaeghere, G. Bihlmayer, T. Björkman, P. Blaha, S. Blügel, V. Blum, D. Caliste, I. E. Castelli, S. J. Clark, A. D. Corso, S. D. Gironcoli, T. Deutsch, J. K. Dewhurst, I. D. Marco, C. Draxl, M. Du, O. Eriksson, J. A. Flores-Livas, K. F. Garrity, L. Genovese, P. Giannozzi, M. Giantomassi, S. Goedecker, X. Gonze, O. Grånäs, E. K. U. Gross, A. Gulans, F. Gygi, D. R. Hamann, P. J. Hasnip, N. A. W. Holzwarth, D. Iusan, D. B. Jochym, F. Jollet, D. Jones, G. Kresse, K. Koepernik, E. Küçükbenli, Y. O. Kvashnin, I. L. M. Locht, S. Lubeck, M. Marsman, N. Marzari, U. Nitzsche, L. Nordström, T. Ozaki, L. Paulatto, C. J. Pickard, W. Poelmans, M. I. J. Probert, K. Refson, M. Richter, G.-M. Rignanese, S. Saha, M. Scheffler, M. Schlipf, K. Schwarz, S. Sharma, F. Tavazza, P. Thunström, A. Tkatchenko, M. Torrent, D. Vanderbilt,

M. J. van Setten, V. V. Speybroeck, J. M. Wills, J. R. Yates, G.-X. Zhang, and S. Cottenier, Science **351**, aad3000 (2016).
[62] H. J. Monkhorst and J. D. Pack, Phys. Rev. B **13**, 5188 (1976).
[63] J. Gebhardt and A. M. Rappe, J. Phys.: Conf. Ser. **921**, 012009 (2017).
[64] A. V. Krukau, O. A. Vydrov, A. F. Izmaylov, and G. E. Scuseria, J. Chem. Phys. **125**, 224106 (2006).
[65] V. Blum, R. Gehrke, F. Hanke, P. Havu, V. Havu, X. Ren, K. Reuter, and M. Scheffler, Comput. Phys. Commun. **180**, 2175 (2009).
[66] FIZ-Karlsruhe, Inorganic Crystal Structure Database (ICSD) (2016).
[67] See Supplemental Material at http://link.aps.org/supplemental/10.1103/PhysRevB.98.125202 for computational details for the binary oxide reference states, ionic radii for all considered ions as well as the resulting crystal and magnetic structures of doped bfo, electronic structure of bfo doped with additional alkali and alkaline-earth metals, influence of the defect charge state on formation energies, further details of the electronic structures for titanium and vanadium doping as well as of the *d* character to bands of group xi dopants, electronic structure of *n*-doped cases employing Zr^{+4}, Ge^{+4}, and Sb^{+4}, and results and discussion for third-row transition-metal dopants.
[68] V. M. Goldschmidt, Naturwissenschaften **14**, 477 (1926).
[69] M. A. Peña and J. L. G. Fierro, Chem. Rev. **101**, 1981 (2001).
[70] P. Ravindran, R. Vidya, A. Kjekshus, H. Fjellvåg, and O. Eriksson, Phys. Rev. B **74**, 224412 (2006).
[71] J. B. Neaton, C. Ederer, U. V. Waghmare, N. A. Spaldin, and K. M. Rabe, Phys. Rev. B **71**, 014113 (2005).
[72] S. J. Clark and J. Robertson, Appl. Phys. Lett. **90**, 132903 (2007).
[73] D. I. Bilc, R. Orlando, R. Shaltaf, G.-M. Rignanese, J. Íñiguez, and P. Ghosez, Phys. Rev. B **77**, 165107 (2008).
[74] K. McDonnell, N. Wadnerkar, N. J. English, M. Rahman, and D. Dowling, Chem. Phys. Lett. **572**, 78 (2013).
[75] V. Shelke, D. Mazumdar, S. Jesse, S. Kalinin, A. Baddorf, and A. Gupta, New J. Phys. **14**, 053040 (2012).
[76] S. R. Basu, L. W. Martin, Y. H. Chu, M. Gajek, R. Ramesh, R. C. Rai, X. Xu, and J. L. Musfeldt, Appl. Phys. Lett. **92**, 091905 (2008).
[77] F. Gao, Y. Yuan, K. F. Wang, X. Y. Chen, F. Chen, J. M. Liu, and Z. F. Ren, Appl. Phys. Lett. **89**, 102506 (2006).
[78] A. G. Gavriliuk, V. V. Struzhkin, I. S. Lyubutin, S. G. Ovchinnikov, M. Y. Hu, and P. Chow, Phys. Rev. B **77**, 155112 (2008).
[79] U. A. Joshi, J. S. Jang, P. H. Borse, and J. S. Lee, Appl. Phys. Lett. **92**, 242106 (2008).
[80] T. Kanai, S.-i. Ohkoshi, and K. Hashimoto, J. Phys. Chem. Solids **64**, 391 (2003).
[81] A. Kumar, R. C. Rai, N. J. Podraza, S. Denev, M. Ramirez, Y.-H. Chu, L. W. Martin, J. Ihlefeld, T. Heeg, J. Schubert, D. G. Schlom, J. Orenstein, R. Ramesh, R. W. Collins, J. L. Musfeldt, and V. Gopalan, Appl. Phys. Lett. **92**, 121915 (2008).
[82] R. Palai, R. S. Katiyar, H. Schmid, P. Tissot, S. J. Clark, J. Robertson, S. A. T. Redfern, G. Catalan, and J. F. Scott, Phys. Rev. B **77**, 014110 (2008).
[83] C. G. Van De Walle and J. Neugebauer, J. Appl. Phys. **95**, 3851 (2004).
[84] H. Choi, D. Shin, B. C. Yeo, T. Song, S. S. Han, N. Park, and S. Kim, ACS Catal. **6**, 2745 (2016).
[85] L. Wang, T. Maxisch, and G. Ceder, Phys. Rev. B **73**, 195107 (2006).
[86] R. D. Johnson III, NIST Computational Chemistry Comparison and Benchmark Database NIST Standard Reference Database Number 101 Release 17b (2015).
[87] A. M. Kolpak, D. Li, R. Shao, A. M. Rappe, and D. A. Bonnell, Phys. Rev. Lett. **101**, 036102 (2008).
[88] G. Henkelman, A. Arnaldsson, and H. Jonsson, Comput. Mater. Sci. **36**, 354 (2006).
[89] A. L. Krick, C.-W. Lee, R. J. Sichel-Tissot, A. M. Rappe, and S. J. May, Adv. Electron. Mater. **2**, 1500372 (2016).
[90] C.-H. Yang, J. Seidel, S. Y. Kim, P. B. Rossen, M. Gajek, Y. H. Chu, L. W. Martin, M. B. Holcomb, Q. He, P. Maksymovych, N. Balke, S. V. Kalinin, A. P. Baddorf, S. R. Basu, M. L. Scullin, and R. Ramesh, Nat. Mater. **8**, 485 (2009).
[91] L. Jiang, S. V. Levchenko, and A. M. Rappe, Phys. Rev. Lett. **108**, 166403 (2012).
[92] N. A. Hill, J. Phys. Chem. B **104**, 6694 (2000).
[93] K. Seeger, *Semiconductor Physics*, 9th ed. (Springer, Berlin, Heidelberg, 2004).
[94] A. F. Holleman, E. Wiberg, and N. Wiberg, *Lehrbuch der Anorganischen Chemie*, 102nd ed. (de Gruyter, Berlin, 2007), pp. 1144 and 1185.